

# Bone Vascularization and Trabecular Bone Formation Are Mediated by PKBalpha/Akt1 in a Gene-Dosage-Dependent Manner: In Vivo and Ex Vivo MRI

Katrien Vandoorne,<sup>1</sup> Jeremy Magland,<sup>5</sup> Vicki Plaks,<sup>1</sup> Amnon Sharir,<sup>3,4</sup> Elazar Zelzer,<sup>3</sup> Felix Wehrli,<sup>5</sup> Brian A. Hemmings,<sup>6</sup> Alon Harmelin,<sup>2</sup> and Michal Neeman<sup>1\*</sup>

**PKBalpha/Akt1, a protein kinase, is a major mediator of angiogenic signaling. The purpose of this study was to determine the role of PKBalpha/Akt1 in bone vascularization and development. For that aim, macromolecular dynamic contrast enhanced MRI was applied to examine in vivo vascular changes in long bones of 40-day-old growing PKBalpha/Akt1-deficient, heterozygous, and wild-type mice. Ex vivo  $\mu$ MRI and  $\mu$ CT were applied to monitor the impact of PKBalpha/Akt1 gene dosage on trabecular bone formation during endochondral bone growth. PKBalpha/Akt1-deficient mice and, remarkably, also heterozygous mice showed significantly reduced blood volume fraction in the humerus compared to wild-type mice. Moreover, PKBalpha/Akt1-deficient mice showed a more severe vascular deficiency with reduced permeability.  $\mu$ CT and  $\mu$ MRI of trabeculae revealed impaired bone formation in both PKBalpha/Akt1-deficient and heterozygous mice, whereas cortical bone parameters were only reduced in PKBalpha/Akt1-deficient mice. Reduction of metaphyseal blood vessel invasion, concomitant with aberrant trabeculae and shorter long bones, demonstrates a gene-dose-dependent role for PKBalpha/Akt1 in regulation of overall size and endochondral bone growth. MRI proved to provide high sensitivity for in vivo detection of subtle gene dose effects leading to impaired bone vascularity and for uncovering changes in trabecular bone. Magn Reson Med 64:54–64, 2010. © 2010 Wiley-Liss, Inc.**

**Key words:** PKBalpha/Akt1; angiogenesis; bone; MRI; CT

<sup>1</sup>Biological Regulation, The Weizmann Institute of Science, Rehovot, Israel.

<sup>2</sup>Veterinary Resources, The Weizmann Institute of Science, Rehovot, Israel.

<sup>3</sup>Molecular Genetics, The Weizmann Institute of Science, Rehovot, Israel.

<sup>4</sup>The Laboratory of Musculoskeletal Biomechanics and Applied Anatomy, Koret School of Veterinary Medicine, Hebrew University of Jerusalem, Rehovot, Israel.

<sup>5</sup>Laboratory for Structural NMR Imaging, Department of Radiology, University of Pennsylvania Health System, Philadelphia, Pennsylvania, USA.

<sup>6</sup>Friedrich Miescher Institute for Biomedical Research, Basel, Switzerland.

Abbreviations:  $-/-$  = gene deficient mice, both alleles of the gene were deactivated;  $+/-$  = heterozygous mice, one allele of the gene was deactivated;  $+/+$  = wild-type mice, both alleles of the gene are present; biotin-BSA-GdDTPA = bovine serum albumin conjugated to biotin and GdDTPA; PKBalpha/Akt1 = protein kinase B alpha, also known as Akt1; PKBgamma/Akt3 = protein kinase B gamma, also known as Akt3; BSA-ROX = bovine serum albumin labeled with rhodamine; H&E = hematoxylin and eosin staining; VEGF = vascular endothelial growth factor; fBV = fraction of blood volume; PS = permeability surface area product; S/C = surface-to-curve ratio; EI = erosion index

\*Correspondence to: Michal Neeman, Ph.D., Department of Biological Regulation, Weizmann Institute of Science, Rehovot 76100, Israel. E-mail: michal.neeman@weizmann.ac.il

Received 26 July 2009; revised 7 December 2009; accepted 20 January 2010.

DOI 10.1002/mrm.22395

Published online in Wiley InterScience (www.interscience.wiley.com).

© 2010 Wiley-Liss, Inc.

Endochondral bone formation, the replacement of avascular cartilage by vascularized bone, is essential for longitudinal bone growth during vertebrate development. During this process, a cartilaginous plate (growth plate) is generated between the shaft of long bones (diaphysis) and their ends (epiphysis). At the cartilaginous epiphyseal plate, sequentially chondrocyte proliferation, hypertrophy, apoptosis, and invasion of vasculature occur, forming primary trabecular bone (1–3). Newly formed blood vessels invade the region between hypertrophic chondrocytes and the newly formed bone matrix at the base of the metaphysis and provide nutrients for the highly specialized cells involved in the regulation of bone formation. Angiogenic growth factors such as vascular endothelial growth factor (VEGF) were shown to affect bone development by triggering blood vessel invasion (3–9). Suppression of VEGF-driven angiogenesis during endochondral bone formation has been shown to impair trabecular bone formation (4).

PKBalpha/Akt1, an intracellular protein kinase, acts downstream of VEGF stimulation of the VEGF receptor in endothelial cells through phosphatidylinositol 3-kinase signaling. PKBalpha/Akt1 is considered to be a major mediator of signaling of angiogenic growth factors, affecting endothelial cell survival, proliferation, and differentiation (4,10). In addition to angiogenesis, PKBalpha/Akt1 regulates many other cellular and physiologic processes, such as glucose metabolism, transcription, cell cycle regulation, survival, and inflammation. PKBalpha/Akt1-deficient mice are smaller, with increased neonatal mortality, along with disordered fetal vasculature and placental hypotrophy (11,12). Moreover, these mice were reported to exhibit bone mineralization defects characterized by decreased length and bone mass of long bones (13,14).

Since postnatal longitudinal bone growth requires infiltration and expansion of the newly formed blood vessels and, on the other hand, PKBalpha/Akt1 mediates intracellular signaling of angiogenesis, we postulated that a vascular deficiency at the site of the long bones could contribute indirectly to impaired bone development in PKBalpha/Akt1-deficient mice. This led us to study postnatally the vascularization and development of long bones in these mice during endochondral bone growth. In particular, in view of the remarkable dose-dependent sensitivity to VEGF signaling during development (heterozygous in-utero mortality of VEGF deficient embryos (15)), we applied here MRI as a sensitive and quantitative tool for comparing the impact of homozygous and heterozygous deficiency of PKBalpha/Akt1.

In this work, we used dynamic contrast-enhanced (DCE) MRI with macromolecular contrast media for quantitative, noninvasive, functional analysis of the microcirculation within the long bones in general and neovascularization of the metaphysis, the growth zone, of growing long bones in particular. In the past, changes in new vessel formation at the growth plate during endochondral bone formation have been evaluated using post-mortem immunohistochemistry (4), evaluating proliferation, apoptosis, and microvessel density. In contrast with immunohistochemistry, macromolecular DCE-MRI provides information on vascular functionality and allows in vivo follow-up. The use of dual-modality contrast material enabled histologic validation of the DCE-MRI data.

Previously, we reported noninvasive MRI, as well as fluorescence microscopy validation of vascular development and associated hyperpermeability in implantation (16), tumors (17), ischemic injury (18), and ovarian xenografts (19), using GdDTPA bound to bovine serum albumin (BSA) and biotin (biotin-BSA-GdDTPA). Recently biotin-BSA-GdDTPA was applied for analysis of bone vascularization during tumor progress (20). Here, we show that biotin-BSA-GdDTPA, because of its selective extravasation from permeable vessels and its slow diffusion and clearance from the extracellular space, allowed high-resolution detection of disturbances of metaphyseal blood flow in PKBalpha/Akt1-deficient mice. This indicates that macromolecular DCE-MRI could be used as an early indicator of impaired vascular function in diseases where altered angiogenesis causes impaired skeletal growth.

Thus, the purpose of this study was to apply MRI as a sensitive, quantitative tool to determine vascular function in the long bones of growing PKBalpha/Akt1-deficient ( $-/-$ ) and heterozygous ( $+/-$ ), mice and to study the impact of PKBalpha/Akt1 gene dosage on trabecular bone formation during endochondral bone growth.

## MATERIALS AND METHODS

### Animals

All animal experiments were approved by the Weizmann Institutional Animal Care and Use Committee. Male PKBalpha/Akt1 wild-type ( $+/+$ ), heterozygote ( $+/-$ ), or knockout ( $-/-$ ) mice were studied by MRI on postnatal day 40. At 40 days of age, PKBalpha/Akt1  $-/-$  were smaller, whereas  $+/-$  were intermediate compared to the  $+/+$  animal size (data not shown). This age was selected for in vivo imaging because animals are still growing, their growth plate is open, and they are more easily accessible for intravenous contrast injection than younger animals.

### Contrast Material

Biotin-BSA-GdDTPA (about 82 kDa) was prepared as reported previously (17) and injected through a tail vein catheter as bolus (0.5 mg/g).

### In Vivo DCE-MRI Studies

The transparency of bones to MRI enabled us to evaluate in vivo the vasculature within the developing long bones. MRI experiments ( $n = 7$  for each group) were performed at 9.4 T on a horizontal Biospec (Bruker, Karlsruhe, Germany), using a linear resonator for excitation and an actively decoupled 2-cm surface coil for detection. Mice were anesthetized (intraperitoneally; 75 mg/kg ketamine, Fort Dodge Laboratories, Fort Dodge, IA; and 3 mg/kg xylazine 2%, VMD, Arendonk, Belgium) followed by subcutaneous addition of about 30% of the initial dose. Anesthetized mice were positioned so that left front leg, and particularly the humerus, was at the center of the surface coil. The tail vein was catheterized with homebuilt catheters fitted with a heparin-washed needle for administration of the contrast media. Body temperature of the animals was controlled using a warming water blanket (Bruker).

At the end of the MRI experiment, 30 min after contrast injection, BSA labeled with rhodamine (BSA-ROX; 1.4  $\mu\text{mol/kg}$ ; Molecular Probes, Eugene, OR), as an early vascular marker, was intravenously injected via a tail-vein catheter 3-5 min prior to animal sacrifice, as reported previously (21).

### DCE-MRI Data Acquisition

Three-dimensional (3D) gradient echo images of the left front limb were acquired before and sequentially for 30 min after intravenous injection of biotin-BSA-GdDTPA. The 3D field of view of the image covered the proximal front limb. A series of variable-flip-angle, precontrast,  $T_1$ -weighted, 3D-gradient-echo images was acquired to determine the endogenous precontrast  $R_1$ . Imaging parameters were precontrast flip angles 5°, 15°, 30°, 50°, and 70°; postcontrast flip angle 15°; pulse repetition time 10 ms; echo time 4 ms; two averages; spectral width 50,000 Hz; matrix 128  $\times$  128  $\times$  64; zero-filled to 256  $\times$  256  $\times$  128; field of view 30  $\times$  30  $\times$  15mm; resolution isotropic 234  $\mu\text{m}$ ; acquisition time 163 sec.

### DCE-MRI Data Analysis

Pixel-by-pixel analysis was done on a personal computer, using MATLAB software (MathWorks Inc., Natick, MA) to generate concentration maps of biotin-BSA-GdDTPA for selected slices containing the humerus of the 3D datasets as described before (17,22). First, precontrast longitudinal relaxation rate ( $R_1$  pre) maps were derived from the variable flip angle data by nonlinear best fit to Eq 1:

$$I = \frac{M_0 \sin \alpha (1 - e^{-TR \times R_1 \text{pre}})}{1 - \cos \alpha \times e^{-TR \times R_1 \text{pre}}} \quad [1]$$

where  $I$  is the signal intensity as a function of pulse flip angle  $\alpha$ , TR is the pulse repetition time (10 ms), and the preexponent term  $M_0$  includes the spin density and the  $T_2$ , which are assumed to be constant. Then, postcontrast  $R_1$  values ( $R_1$  post) were calculated from the precontrast and postcontrast signal intensities ( $I_{\text{pre}}$  and  $I_{\text{post}}$ ).

respectively, acquired with a flip angle of  $15^\circ$ ). Finally, concentration maps were calculated based on the relaxivity of biotin-BSA-GdDTPA ( $r$ ,  $99 \text{ mM}^{-1} \text{ sec}^{-1}$  per BSA, at 9.4 T) (17,22).

During the first 15 min after administration of the contrast media, its concentration in circulation was stable (21) and contrast accumulation was linear in regions of permeable vasculature but not yet noticeably affected by interstitial convection (22). Therefore, linear regression of the dynamic change in concentration during the first 15 min postcontrast was used for the derivation of two vascular parameters, for selected regions of interest (ROIs), the humerus, and for each pixel in parametric maps (21) (Fig. 3b). The blood volume fraction (fBV) was derived from the ratio between the extrapolated concentration of biotin-BSA-GdDTPA at the time of administration and the concentration in the blood calculated from mean concentration values at selected ROIs within the cephalic vein. The permeability surface area product (PS;  $\text{minutes}^{-1}$ ) is derived from the initial rate of accumulation of the contrast material at a selected ROI containing the left humerus, enhancing between 0 and 15 min, normalized to the initial blood concentration. PS reflects the extravasation of macromolecules such as albumin from blood vessels and their accumulation in the tissues.

Numeric values for fBV and PS were calculated by selecting ROIs that delineate the humerus. For presentation of parametric maps (Fig. 3), the stacks of fBV maps (generated for slices of interest) were projected to show the mean value in each pixel in the axial plane.

#### Histology, Immunohistochemistry and Fluorescence Microscopy

For histologic validation of the DCE-MRI, dual labeling was performed using BSA-ROX and biotin-BSA-GdDTPA. The right humeri of 40-day-old mice were fixed (Carnoy's solution for fluorescence), decalcified and embedded in paraffin, sectioned serially at  $4\text{-}\mu\text{m}$  thickness, and stained for the biotinylated contrast agent with avidin-fluorescein isothiocyanate (FITC) (Molecular Probes) as previously described (21). BSA-ROX injected just before collection of the tissue remained intact throughout the processing mentioned above. For immunohistochemistry, tissue samples were fixed in 4% paraformaldehyde, decalcified, and embedded. Subsequently, tissue sections were stained with anti-CD34 (Cedarlane Laboratories, Burlington, Ontario, Canada). For hematoxylin and eosin (H&E) staining (histomorphometric analysis), the right humeri ( $n = 4$  for each group) were fixed in 4% PFA, decalcified, embedded, and stained with H&E.

#### Morphometric Analysis of Histologic Sections

H&E-stained histologic sections of bone were analyzed by basic stereological approach (23). For each group ( $n = 4$ ), decalcified H&E sections of the humerus (two to three sections per animal) were imaged with an Eclipse E800 microscope and analyzed by computer-assisted image analysis, using Image Pro Plus 5.0 Software (Media Cybernetics, Bethesda, MD; Eclipse E800 microscope

connected to Nikon Digital Camera DXM 1200, Nikon, Tokyo, Japan). The proximal humerus was studied not more than  $500 \mu\text{m}$  distal to the growth plate (distal to the zone of calcification). A grid was placed on square fields of  $<0.25\text{mm}^2$  for each section and each parameter, producing a particular point count. For quantitative image analysis, three parameters were measured: (i) the percentage of trabeculae, which represents the number of points on the grid corresponding to trabeculae, divided by the total number of points (trabeculae representing bone matrix, calcified cartilage matrix with osteoblasts, and osteoclasts); (ii) the percentage of blood vessels (sinusoids, delimited by endothelial cells containing red blood cells); and (iii) the percentage of bone marrow (interspersed between trabeculae and blood vessels containing cells of blood cell synthesis), calculated the same way.

#### Bone Morphometric Analysis by $\mu\text{CT}$ and $\mu\text{MRI}$ Analysis

##### $\mu\text{CT}$

Left humeri of ( $n = 4$  for each group) were dissected, cleaned, and stored at  $-20^\circ\text{C}$  until tested. Bones were thawed at room temperature and scanned by CT (eXplore Locus SP; GE Healthcare, London, Ontario, Canada) with 80-kV x-ray voltage,  $80\text{-}\mu\text{A}$  current, and 400-ms integration time. Three-dimensional  $8\text{-}\mu\text{m}$  isotropic images were obtained using  $\mu\text{CT}$ . Images were reconstructed and thresholded to distinguish bone voxels with MicroView software, version 5.2.2 (GE Healthcare). Analysis of cortical bone (bone mineral density, bone mineral concentration, and mean thickness) was performed on a transverse section of the diaphysis equivalent to 3.5% of the whole bone length, starting immediately adjacent and distally to the deltoid tuberosity. Analysis of trabecular bone was performed on a transverse section of the metaphysis equivalent to 3% of the whole bone length, starting immediately adjacent and distally to the growth plate. ROIs consisted of the proximal metaphyseal region and were used for measurement of bone volume fraction, number of trabeculae, and their spacing.

##### $\mu\text{MRI}$

Trabecular bone was also measured by  $\mu\text{MRI}$  of the femur. Femora of the same mice as for  $\mu\text{CT}$ , were used, and for each group one extra animal was added ( $n = 5$  for each group). The bones were placed in 5mm NMR tubes with 1.5-mM Gd in saline, placed under vacuum to eliminate air bubbles, and imaged at 9.4 T with fast low angle shot (FLASH) 3D on a vertical-bore Avance III DRX 400-MHz NMR spectrometer (Bruker), equipped with microimaging probe and a 5mm insert coil. Images of distal femora of these mice were acquired with following imaging parameters: flip angle  $15^\circ$ ; pulse repetition time 15 ms; echo time 3.3 ms; four averages; spectral width 100,000 Hz; matrix  $512 \times 256 \times 512$ ; field of view  $10 \times 5 \times 10\text{mm}$ ;  $20\text{-}\mu\text{m}$  isotropic resolution.

Data were analyzed by the virtual bone biopsy processing algorithm (24). The 3D datasets were first segmented by hand to obtain the trabecular bone region of interest. A custom user interface was used for this purpose,

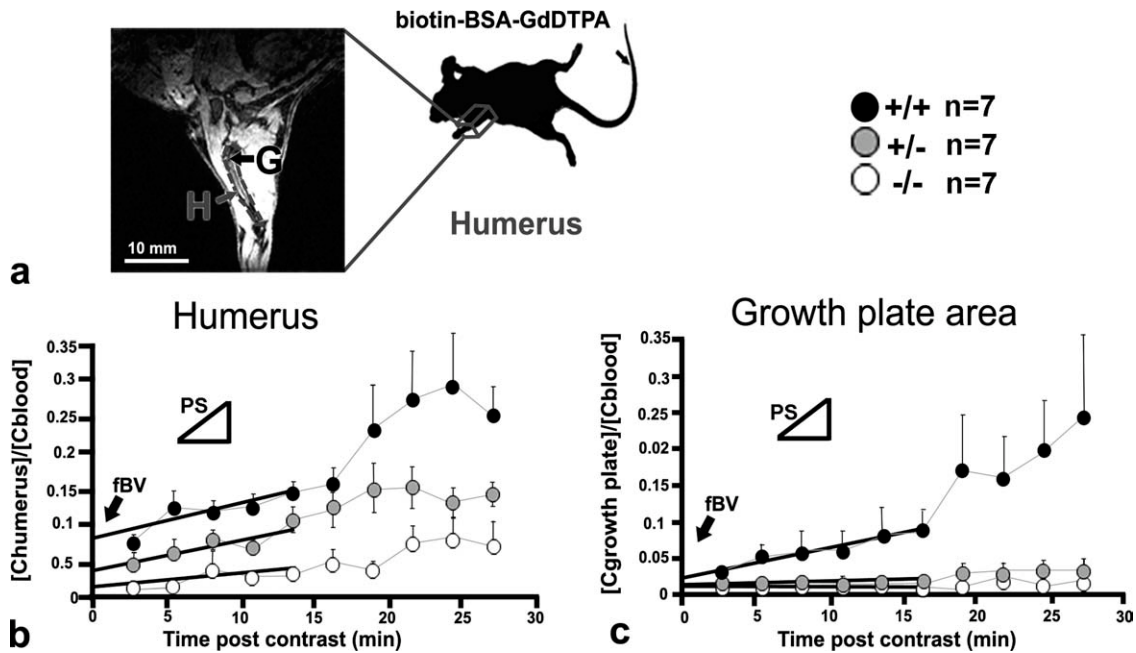


FIG. 1. In vivo DCE-MRI of the role of PKBalpha/Akt1 in bone vascularization. **a:** Consecutive MRI images of the front limb of growing male mice were acquired before and after administration of macromolecular contrast material (biotin-BSA-GdDTPA; intravenous, via a tail vein catheter). MRI slice showing the humerus (H) and the growth plate area (G) as the ROIs for analysis. **b:** DCE-MRI for 30 min after contrast injection (10 time points) of the humerus normalized with contrast concentration in the cephalic vein at each time point. **c:** Dynamic 3D imaging included follow-up of contrast enhancement for 30 min postcontrast (10 time points) for the area of the growth plate. For both **(b)** and **(c)**, fBV (intercept with time 0) and PS (the slope) values were calculated from a linear regression of the first 15 min for each group. (–/– = PKBalpha/Akt1 knockout; +/- = heterozygote; +/+ = wild type;  $n = 7$  for each group).

which allowed the user to manually outline the trabecular bone region (using polygons) in a few axial reference slices. The program then linearly interpolated between the reference slices to achieve a 3D segmentation. The segmented volume was then subjected to the virtual bone biopsy processing algorithm, comprising the following steps: (1) correction for coil shading; (2) inversion, interpolation, and binarization; (3) 3D skeletonization; and (4) topological classification via digital topological analysis.

The digital topological analysis step results in a voxel-by-voxel classification of the 3D skeleton into plates, rods, and junctions of various types. From these, composite structural parameters surface-to-curve ratio (S/C) and erosion index (EI) were obtained. The S/C is an estimation of the number of platelike voxels divided by the number or rodlike voxels in the skeleton. It is generally understood that the trabecular network's strength is impaired when plates are more eroded and converted into rods. Therefore, a higher S/C value suggests stronger bone. EI is a similar parameter, also a ratio of the sum of parameters expected to increase with reduced trabecular network's strength divided by the sum of those expected to decrease. Therefore, lower EI suggests stronger bone.

Since the distal femora varied widely in terms of length and shape, the use of objective criteria for selecting the portion of the bone to be analyzed was required. While the cross-sectional segmentation was straightforward to perform manually, the choice of longitudinal region of interest was less clear. Therefore, in

each sample, the 30 contiguous slices with highest bone volume fraction were automatically selected for analysis, and the parameters were computed only over these slices.

#### Statistical Analysis

One-way ANOVA was used for the analysis of significance of different parameters of the three groups, PKBalpha/Akt1 +/+, +/-, and -/- mice. When the differences were found statistically significant ( $P < 0.05$ ), post hoc test was performed using Tukey's Honestly Significant Difference test to control for familywise error rate. The mean value  $\pm$  standard deviation is described for each group.

## RESULTS

### PKBalpha/Akt1 Controls Bone Vascularization in a Gene-Dosage-Dependent Manner

fBV and PS in the humerus and its proximal growth plate were measured in vivo by DCE-MRI using pharmacokinetic analysis of macromolecular biotin-BSA-GdDTPA. Two ROIs were analyzed (Figs. 1, 2) and pixel-by-pixel analysis was done (Fig. 3) to derive values and maps of blood volume (fBV) and vessel permeability (PS). The first ROI, the humerus (Fig. 1a,b), a highly vascularized long bone, showed a high initial contrast enhancement, reflected by a high fBV in the wild type ( $0.0785 \pm 0.013$ ). The fBV was significantly reduced in PKBalpha/Akt1-deficient (-/-) and heterozygous (+/-)

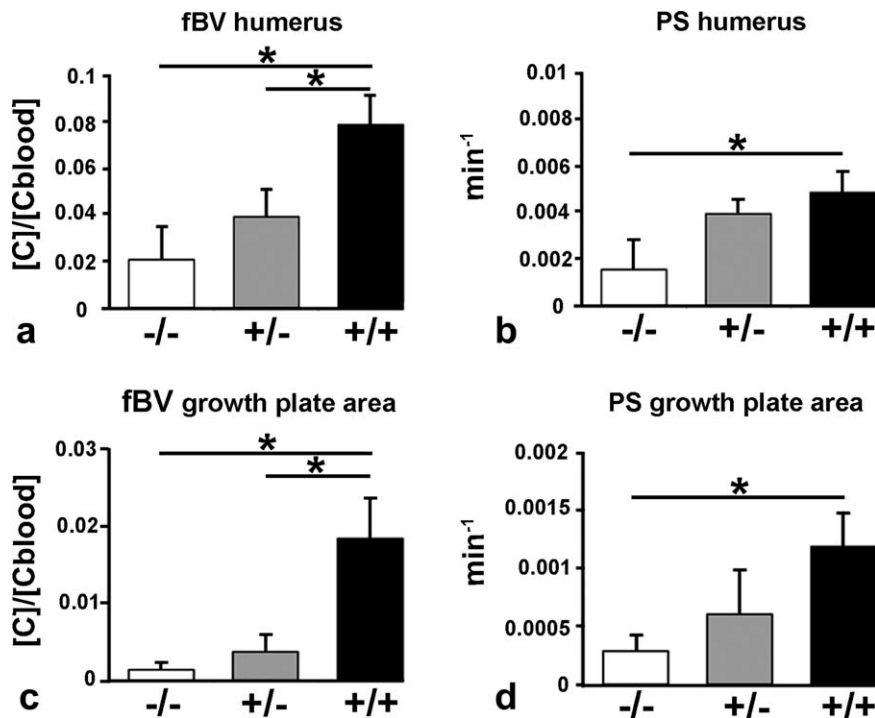


FIG. 2. Quantification of vascular MRI parameters in PKBalpha/Akt1 bones calculated from a linear regression of the first 15 min in DCE-MRI. **a,c**: fBV and **(b,d)** PS of the humerus **(a,b)** and the region of the proximal growth plate of the humerus **(c,d)**. **a,c**: fBV: the ratio between the extrapolated concentration of biotin-BSA-GdDTPA at the time of administration and the concentration in the blood. This parameter indicates the fraction of blood volume in the tissue. **b,d**: PS: the slope of this linear regression (minutes<sup>-1</sup>), measuring the extravasation of macromolecules out of blood vessels (mean  $\pm$  standard deviation; \*  $P < 0.05$ ; -/- = PKBalpha/Akt1 knockout; +/- = heterozygote; +/+ = wild type;  $n = 7$  for each group).

mice compared to the wild-type mice ( $0.0207 \pm 0.014$  and  $0.0392 \pm 0.012$ , respectively; Fig. 2a). This result indicates gene-dosage-dependent effects with reduced (micro)vascular density not only within the humerus of PKBalpha/Akt1 -/- but remarkably also in PKBalpha/Akt1 +/- mice.

The slope of the linear regression of the first 15 min, the PS (Fig. 1a), showed contrast accumulation over time due to high vascular permeability of sinusoids in the bone in wild-type mice ( $0.0049 \pm 0.0009 \text{ min}^{-1}$ ). The PS was significantly reduced in PKBalpha/Akt1 -/- ( $0.0017 \pm 0.0007 \text{ min}^{-1}$ ). No significant difference in PS was found in +/- relative to wild-type mice (Fig. 2b). The concentration of contrast agent in the blood remained constant over the first 15 min, and no difference in dynamics or concentration was found between the groups (data not shown). The slope of the contrast behavior curve of the later data points after 15 min was only significantly different for PKBalpha/Akt1 +/- mice, though each separate time point of PKBalpha/Akt1 -/- mice after 15 min was significantly different from PKBalpha/Akt1 +/+ mice. Heterozygous PKBalpha/Akt1 +/- mice showed significantly different contrast changes for the two last time points and showed intermediate behavior at earlier time points (16–22 min).

The second ROI analyzed, the proximal growth plate region of the humerus (Fig. 1c), showed lower initial contrast enhancement and thus appeared to be less vascularized than the whole bone (fBV;  $0.0184 \pm 0.0050$ ). The lower fBV values are consistent with inclusion of the avascular epiphyseal plate in this ROI. The fBV was significantly decreased in PKBalpha/Akt1 -/- and +/- mice ( $0.0014 \pm 0.0008$  and  $0.0037 \pm 0.0021$ , respectively) compared to the wild-type mice, indicating reduced (micro)vascular density in the area of the epiphyseal plate of -/- and +/- mice (Fig. 2c). Vascular

permeability (PS) derived from the first 15 min showed the same contrast accumulation over time as over the whole humerus, although the value for the wild types ( $0.0012 \pm 0.0003 \text{ min}^{-1}$ ) was lower than for the entire humerus. The PS was significantly reduced in PKBalpha/Akt1 -/- mice ( $0.0003 \pm 0.0001 \text{ min}^{-1}$ ), but no significant difference in permeability was found in +/- mice (Fig. 2d) relative to wild-type mice. The linear regression of the first 15 min postcontrast was used for calculation of fBV (Fig. 1b) on a pixel-by-pixel basis and generation of fBV and PS maps showing a reduced (micro)vascular density in both PKBalpha/Akt1 -/- and +/- humeri (Fig. 3).

#### Biodistribution of Macromolecular Contrast Agent, Immunohistochemistry, and Microscopic Validation by Histomorphometric Analysis of the Proximal Humeral Metaphysis of PKBalpha/Akt1 40-Day-Old Mice

Histologic staining of biotin-BSA-GdDTPA was used for validation of the microscopic biodistribution of the contrast material within the humerus. Elevated accumulation of biotin-BSA-GdDTPA was demonstrated beneath the epiphyseal plate (G; Fig. 4), corresponding to the high permeability of the sinusoid blood vessels in the bone of wild-type mice, as revealed with DCE-MRI. Large blood vessels could be observed by BSA-ROX staining as an early vascular marker (Fig. 4b,c). Reduced vessel density was seen in PKBalpha/Akt1 -/-, as well as +/- (Fig. 4c), matching with a reduced (micro)vascular density in these humeri detected in vivo by MRI (Figs. 1, 2). In addition, microvasculature was evaluated using the CD34 monoclonal antibody, pointing out newly formed blood vessels and capillaries distally to the epiphyseal plate (Fig. 4d). Using similar exposure time, no fluorescence could be detected in sections from PKBalpha/Akt1

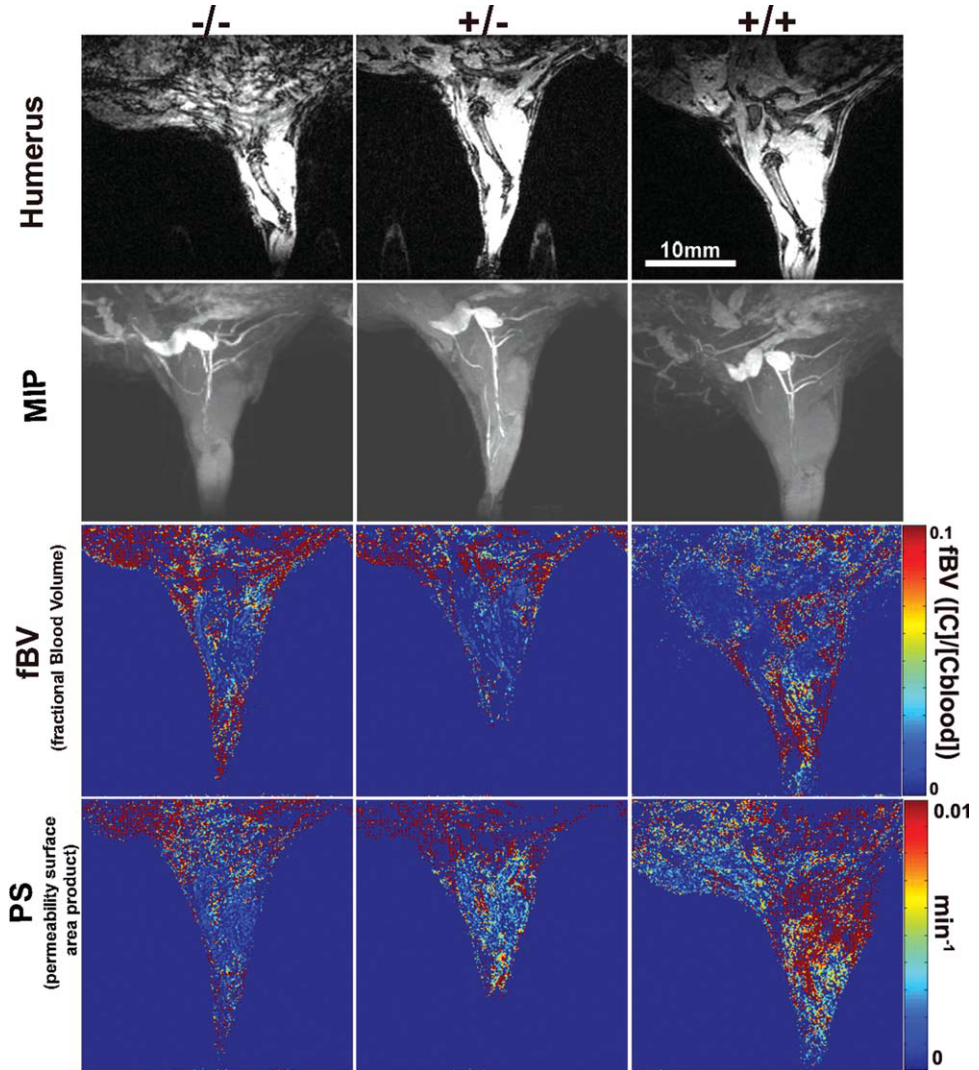


FIG. 3. Mapping vascular parameters in PKBalpha/Akt1 mice by DCE-MRI. Single sections derived from 3D gradient echo data containing the humerus, MIP, fBV maps, and PS maps. Linear fit of the first 15 min (trend lines, see Fig. 1) was used for derivation of fBV and PS (fBV = tissue concentration at time 0 divided by blood concentration; [C] = tissue concentration of contrast agent at time 0; [Cblood] = blood concentration of contrast agent at time 0; PS = the slope of the normalized contrast concentration).

$-/-$  mice, whereas sections from PKBalpha/Akt1  $+/-$  mice showed intermediate signal.

Histomorphometric analysis of the left proximal humeral metaphysis (Fig. 5) revealed lower trabecular bone and lower blood vessels density, along with elevated bone marrow content, in both PKBalpha/Akt1  $-/-$  and  $+/-$  relative to  $+/+$  mice, while no significant difference was found between PKBalpha/Akt1  $+/-$  and  $-/-$  (Fig. 6). These results are consistent with the reduced (micro)vascular density observed by DCE-MRI (Figs. 1–3). In addition, humeral length of 40-day-old PKBalpha/Akt1  $-/-$  mice was significantly reduced compared to  $+/+$  length, whereas  $+/-$  humeral length was significantly different from both  $-/-$  and  $+/+$  and intermediate between both (data not shown).

#### PKBalpha/Akt1 Controls Trabecular Bone Sedimentation and Structure in a Gene-Dosage-Dependent Manner

Since sedimentation of minerals, and thus formation of new bone, occurs at the growth plate through metaphyseal blood vessels, giving rise to trabeculae, we focused on trabecular bone analysis.  $\mu$ CT images of left humeri (Fig. 5b) showed impaired trabecular bone parameters at the proximal metaphysis at the diaphysis in PKBalpha/

Akt1  $-/-$  and  $+/-$  mice. Cortical bone parameters were found only significantly different in PKBalpha/Akt1  $-/-$  mice. Trabecular bone analysis revealed a lower bone volume fraction, a lower trabecular number, and a higher trabecular separation in both PKBalpha/Akt1  $-/-$  and  $+/-$  mice. In addition, cortical bone showed decreased bone mineral density, mid-diaphyseal cortical thickness, and bone mineral density in  $-/-$ , but no reduction was demonstrated in  $+/-$  (Fig. 7; Table 1).

Trabecular bone of the right femur (Fig. 5c) was subsequently examined by  $\mu$ MRI, to validate the findings in the humerus. A major determinant of trabecular bone strength is orientation and is used for understanding the implications of osteoporotic bone loss in clinics (24). While CT is more sensitive to mineralized bone,  $\mu$ MRI shows particular sensitivity to the confinement of water within the developing trabecular bone. MRI microscopy of the femur depicted the trabecular bone within the epiphysis and metaphysis. Composite structural parameters (S/C and EI) were obtained by subjecting segmented volumes of the distal femoral metaphysis to the virtual bone biopsy processing algorithm. The femoral metaphysis of PKBalpha/Akt1  $-/-$  mice, and notably also  $+/-$  mice, showed significantly more rodlike than platelike

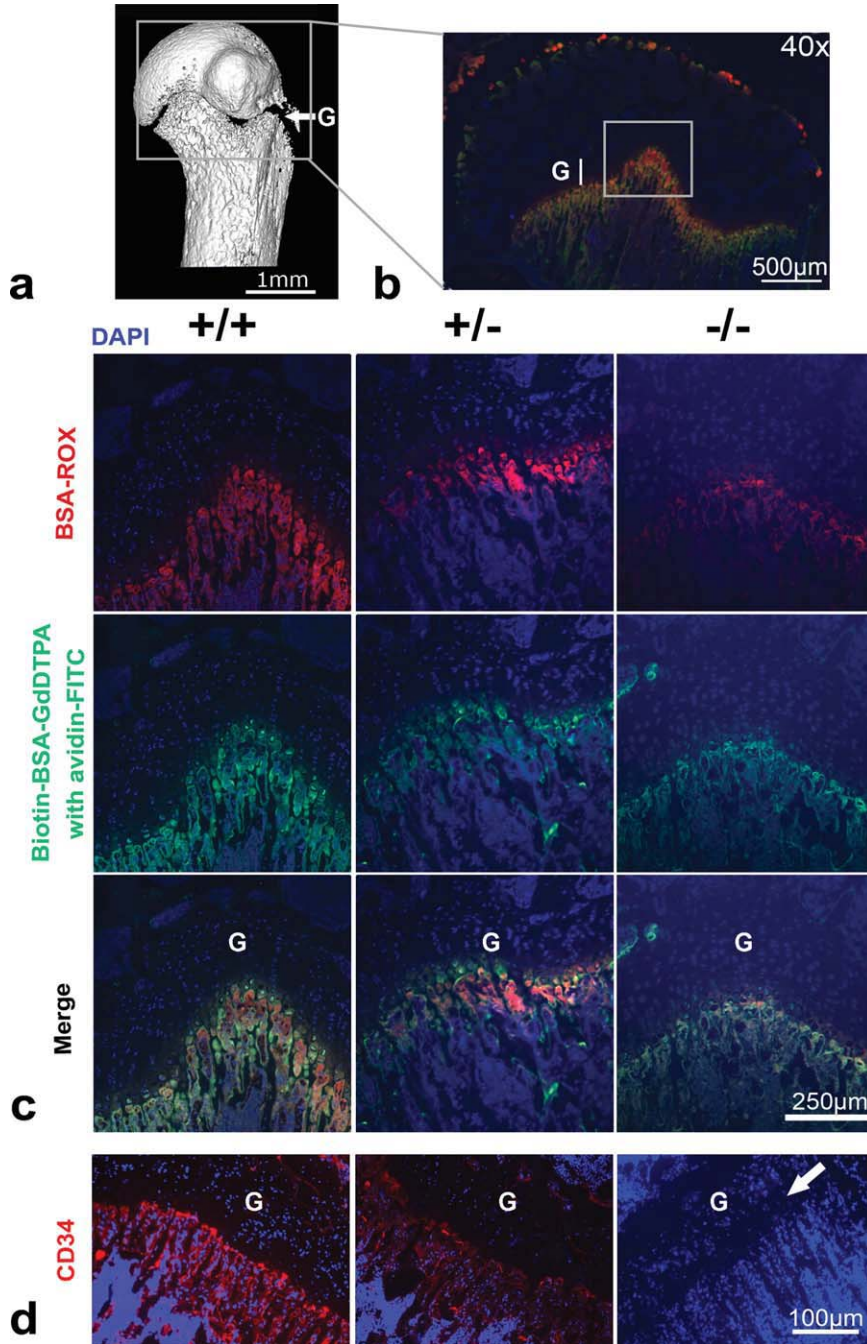


FIG. 4. Microscopic histologic analysis of the distribution of the macromolecular contrast agent. **a:** (Left) Surface projection  $\mu$ CT of wild type proximal humerus (see also Fig. 7) indicating the growth plate (G) separating the proximal epiphysis and metaphysis of the humerus. **b:** Composite image of 40 $\times$  magnification of wild-type proximal humerus indicating the region shown in **(c)** containing the epiphysial plate (G). Tissues were retrieved 30 min after injection of biotin-BSA-GdDTPA (green; stained for biotin using avidin-FITC), and immediately after injection of BSA-ROX (red). **c:** Blood vessels only are stained with BSA-ROX (red; top row), whereas biotin-BSA-GdDTPA (green; central row) partly leaked out of the sinusoids close to the growth plate (G). **d:** CD34 staining for newly formed blood vessels and capillaries. PKBalpha/Akt1-deficient metaphysis ( $-/-$ ) shows no staining of CD34 in an exposure time that gives in wild-type ( $+/+$ ) staining distal to the growth plate (G). Heterozygous ( $+/-$ ) staining is intermediate between  $+/+$  and  $-/-$  (arrow in the  $-/-$  panel indicates an area where low fluorescence could be detected at a higher exposure time, which oversaturated the fluorescent signal of the  $+/+$  section).

morphology, which translates into decreased S/C compared with  $+/+$ . An increased EI, which indicates more perforated trabecular plates, was observed in the trabecular network of PKBalpha/Akt1 null and heterozygote, while no difference was seen between heterozygote and knockout. These substantial changes in trabecular architecture of the metaphysis of the distal femur, in particular as they relate to topology of the network, were detected between PKBalpha/Akt1  $-/-$  and  $+/-$  as compared to  $+/+$  mice, implicating reduced trabecular bone strength in null and heterozygote mice and suggesting a significant gene-dosage-dependent role for PKBalpha/Akt1 in bone development (Fig. 7; Table 1).

## DISCUSSION

Vascular development is critical for elongation of the long bones and thereby is an important factor in determination of the individual size. We have shown here that macromolecular DCE-MRI provides a sensitive method for detection of impaired vascular function in the humerus. We described deficient vascularization of the humeral metaphysis of the growth plate in PKBalpha/Akt1 knockout ( $-/-$ ) and heterozygote ( $+/-$ ) mice, which could be detected *in vivo* by macromolecular DCE-MRI. In addition, as it is known that new bone formation follows angiogenesis, we showed in both

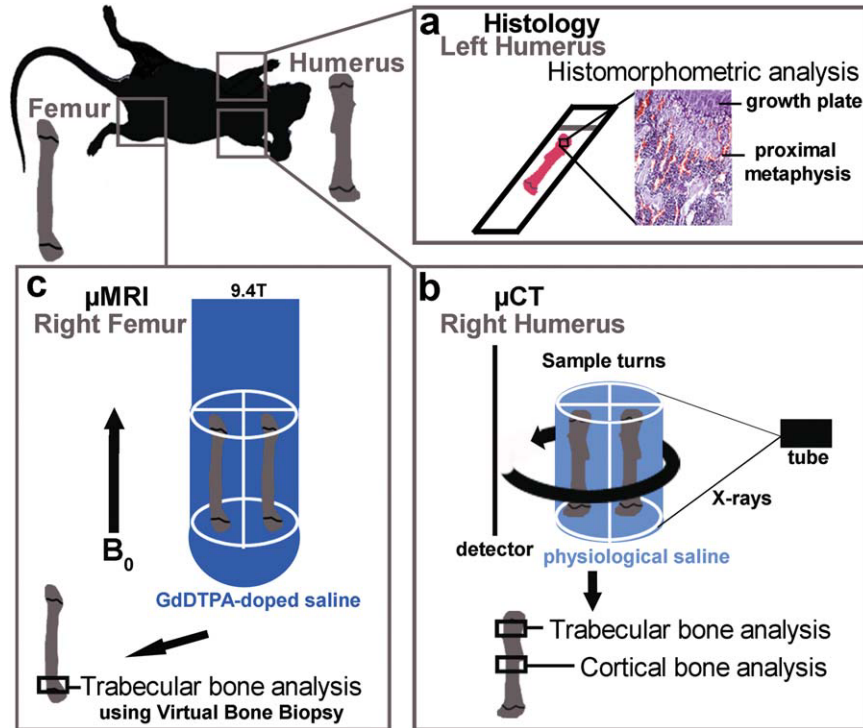


FIG. 5. Setup of  $\mu$ CT and  $\mu$ MRI analysis of the bone architecture. **a:** For histology, humeri were cleaned, fixed, decalcified, embedded in paraffin, sectioned, and stained with H&E. Histomorphometric analysis was performed on H&E slides of the left proximal metaphysis (region just beneath the growth plate) of the left humerus (see Fig. 6). **b:** For  $\mu$ CT, right humeri were cleaned of soft tissue and stored at  $-20^{\circ}\text{C}$ . After thawing at room temperature, bones were placed with four bones in a sample holder, immersed with physiologic saline and immobilized with foam rubber, and scanned. Right proximal metaphyseal area and cortical area of the humeri were used for trabecular and cortical bone analysis, respectively (see Fig. 7 and Table 1). **c:** As an alternative analysis of trabecular bone, right femora were taken for  $\mu$ MRI. They were cleaned, placed in 5mm NMR tubes and immersed with 1.5-mM GdDTPA in saline and placed under vacuum to eliminate air bubbles. The bones were imaged at vertical 9.4-T magnet, and the distal metaphyseal trabeculae were characterized using a virtual bone biopsy processing algorithm (see Fig. 7 and Table 1).

PKBalpha/Akt1  $+/-$  and  $-/-$  deficient metaphyseal trabeculae, probably due to a deficient supply of minerals and specialized cells.

Noninvasively quantifying vascular function and identifying vascular defects at the growth plate of long bones in living animals gives access to important dynamic information that could not be obtained using classical methods, such as histology. Because of its high molecular size, biotin-BSA-GdDTPA acts as a blood pool agent and can only extravasate from leaky vessels. This improves the specificity for detection of small changes in blood volume and vascular permeability. Macromolecular and low-molecular-weight DCE-MRI have been used in previous studies as a valid and noninvasive method for semiquantitative evaluation of microcirculation in bone pathologies with increased circulation such as solid tumors and bone marrow disease (20,25–27) but has not been described in evaluation of decreased circulation in bones, associated with genetic defects leading to developmental growth retardation.

In long bones such as the humerus and femur, the main blood supply is the diaphyseal artery (entering through a single nutrient foramen; Fig. 7a) and the metaphyseal, epiphyseal, and periosteal arterial networks. In the growing long bone, leakiness of the blood vessels includes both the newly formed blood vessels near the

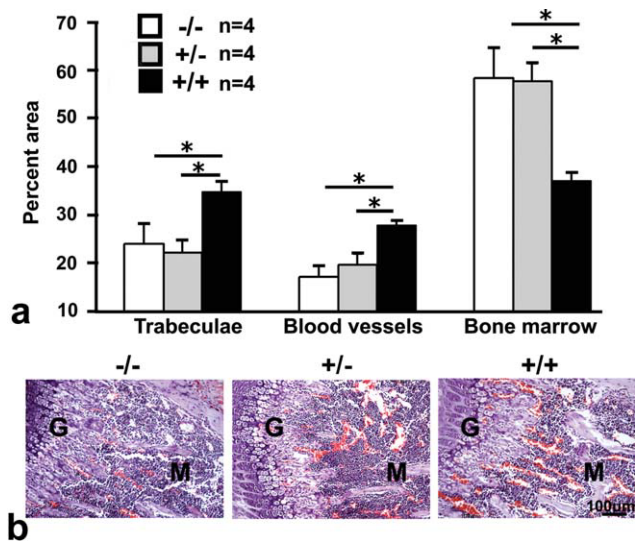


FIG. 6. Histologic analysis of hypovascularity in humeri of male 40-day-old PKBalpha/Akt1 mice. **a:** Histomorphometric analysis on **(b)** H&E histologic slices of the left proximal metaphysis of the humerus (mean  $\pm$  standard deviation; \*  $P < 0.05$ ;  $-/-$  = PKBalpha/Akt1 knockout;  $+/-$  = heterozygote;  $+/+$  = wild type;  $n = 4$  animals for each group, two to three sections per animal; G = growth plate; M = metaphysis).

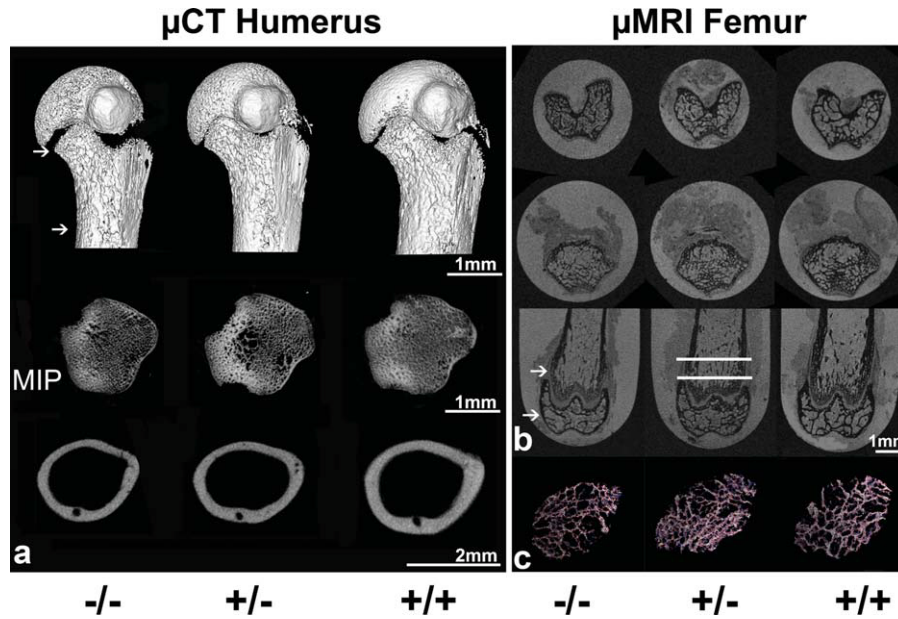


FIG. 7. Ex vivo bone analysis of 40-day-old male mice **(a)**  $\mu$ CT analysis of proximal humerus. Upper panel, surface projection; metaphysis (upper arrow); diaphysis (lower arrow). Middle panel, MIP of metaphyseal trabeculae of the humerus (ROI for analysis). Lower panel, cortical bone at mid-diaphysis showing the nutrient foramina. **b:** Distal femora of the same animals imaged by  $\mu$ MRI. Arrows on the longitudinal view (lower) show the region of the epiphysis and metaphysis; slices of MR images of the epiphysis (upper) and metaphysis (middle) illustrate the trabecular bone. The region analyzed by virtual bone biopsy is shown between two lines (see Table 1). **c:** Surface renderings of the metaphyseal region viewed from the top. Skeletonization converts plates to surfaces (white, surface edges red) and rods to curves (blue).  $\mu$ MRI of trabecular bone of the femoral metaphysis was analyzed using the virtual bone biopsy (see Table 1).

growth plate and the sinusoids in the entire long bone (28). This permeability is evident in the behavior of the contrast agent during the first 15 min. Unlike other tissues with permeable vasculature, lymphatics are not present in bone tissue (29), and thus contrast behavior is not characterized by lymphatic drain. Furthermore, the last branches of the nutrient artery to the metaphysis in growing bone loop very sharply and empty into a large sinusoidal system where the rate of blood flow is decreased. This slow flow at the metaphysis of growing bone is illustrated in osteomyelitis in children, where bacteria in circulation can easily lodge at the metaphysis with slow blood flow (30). After 15 min, the macromo-

lecular contrast accumulated further in the bone. This accumulation is unique to the bone and can be explained by a complex interplay of continuous deposition in sinusoids, convection, and slow clearance of contrast agent.

In this work, macromolecular DCE-MRI proved to be sensitive for measuring impaired vascular function at the humerus of PKBalpha/Akt1  $-/-$  and  $+/-$  mice. fBV, a measure for (micro)vascular density, in the humerus and its growth plate area was found to be significantly reduced in  $-/-$  and  $+/-$  mice. Furthermore, PS was reduced in  $-/-$  mice. The results were validated by fluorescence microscopy, revealing reduced localization of

Table 1  
Ex Vivo  $\mu$ CT and  $\mu$ MRI Analysis of PKBalpha/Akt1 Long Bones

	$-/-$	$+/-$	$+/+$
$\mu$ CT humerus ( $n = 4$ for each group) trabecular bone analysis			
Bone volume fraction	$0.243 \pm 0.018^*$	$0.256 \pm 0.023^*$	$0.410 \pm 0.007$
Trabecular number	$7.8 \pm 1.5^*$	$7.4 \pm 0.6^*$	$14.6 \pm 1.7$
Trabecular separation ( $\mu$ m)	$117 \pm 9^*$	$108 \pm 25^*$	$42 \pm 4$
Cortical bone analysis			
Mean thickness (mm)	$0.096 \pm 0.006^*$	$0.120 \pm 0.005$	$0.132 \pm 0.004$
Bone mineral density (mm/cc)	$929 \pm 30^*$	$999 \pm 12$	$1038 \pm 17$
Bone mineral concentration ( $\mu$ g)	$2.1 \pm 0.2^*$	$2.8 \pm 0.1$	$3.3 \pm 0.2$
$\mu$ MRI femur ( $n = 5$ for each group) trabecular bone analysis			
S/C	$4.11 \pm 0.59^*$	$3.79 \pm 0.65^*$	$6.24 \pm 0.20$
EI	$1.14 \pm 0.18^*$	$1.11 \pm 0.12^*$	$0.69 \pm 0.03$

$-/-$  = PKBalpha/Akt1 knockout;  $+/-$  = heterozygote;  $+/+$  = wild type; mean  $\pm$  standard deviation

\*Significantly different from the wild type ( $+/+$ );  $P < 0.05$ .

the BSA-ROX an early vascular marker distal from the growth plate, and also less MR contrast agent where newly formed metaphyseal blood vessels appeared leaky. After 15 min, the contrast accumulates continuously, also in +/- and -/- mice, but to a lesser extent than in +/+ mice. These results indicate impaired vascular function in +/- and even more severe impairment in PKBalpha/Akt1 -/- mice.

Blood supply in the bone is necessary for sufficient deposition of minerals and provision of highly specialized cells for bone formation, and more particularly for trabecular bone formation near the growth plate (4). In PKBalpha/Akt1 -/-, osteopenia was previously described (14), but impaired bone formation in PKBalpha/Akt1 +/- mice has not been reported. Our results, of two separate long bones, using both  $\mu$ CT and  $\mu$ MRI show significantly reduced trabecular bone formation in +/- as well. Cortical bone parameters in +/- appeared not reduced compared to +/+ bones. This complies with the less severe vascular phenotype of +/- at the humerus. Dosage-dependent effects of PKBalpha/Akt1 on animal survival and development have been described previously only on the background of PKBgamma/Akt3 -/- mice (31).

Previously, growth retardation (12) and in utero lethality (11) of PKBalpha/Akt1 -/- mice were reported and attributed independently to placental hypovascularity (32) or to osteopenia (13,14). PKBalpha/Akt1 is predominantly expressed in endothelial cells and is a central mediator in signaling of angiogenesis (33). Reduced angiogenesis at growth plates, loss of metaphyseal blood vessels, and consequent reduction in trabecular bone formation have been shown in studies of inhibition of VEGF signaling (4). VEGF expressed by hypertrophic chondrocytes mediates blood vessel invasion into the zone of hypertrophic cartilage (34), and this infiltration of endothelial cells boosts the functional differentiation of other cells, particularly osteoblast and osteoclasts (9). Reduction in trabecular bone mass and defects in osteoblasts and osteoclasts have already been demonstrated in PKBalpha/Akt1 -/- mice (14). Moreover, a substantial reduction in monocyte-derived chondroclasts that are tartrate-resistant acid phosphatase positive cells was previously reported in PKBalpha/Akt1-deficient mice (14), as was also seen in inhibition of VEGF signaling, indicating impaired recruitment of these specialized cells due to reduced neovascularization at the growth plate (4). A recent study (13) showed decreased VEGF immunostaining at the site of new bone formation, suggesting a possible role for PKBalpha/Akt1 in angiogenesis. Nevertheless, no quantitative measurements of newly formed blood vessels were provided, and +/- and +/+ were taken together as control group for -/- mice.

In summary, we showed here significant vascular defects using the humerus, in particular of metaphyseal blood vessels, in both PKBalpha/Akt1-deficient and heterozygote mice. In addition, loss of a single allele of PKBalpha/Akt1 was sufficient to affect bone vessel density at the epiphyseal plate region and (micro)vascular density of the long bone. We confirmed reduced trabecular and cortical bone formation in PKBalpha/Akt1-null

mice. Moreover, we show that trabeculae were aberrant in growing PKBalpha/Akt1 heterozygote mice, underscoring the gene-dosage-dependent regulation of endochondral bone growth by PKBalpha/Akt1. MRI was instrumental for analysis and quantification of vascular function in the growing bone and for analysis of trabecular bone mineralization.

## ACKNOWLEDGMENTS

We would like to thank Itzhak Ino from the Animal Facility for animal husbandry, Tamara Berkutzki for help with the histomorphometric analysis, Peter Bendel for MRI support, Yoseph Addadi for technical help and stimulating discussions and Yisrael Parmet for statistical help. This work was supported by the 7th Framework European Research Council Advanced Grant 232640-IMAGO (to M.N.). Michal Neeman is the incumbent of the Helen and Morris Mauerberger Chair.

## REFERENCES

- Karsenty G. The genetic transformation of bone biology. *Genes Dev* 1999;13:3037-3051.
- Olsen BR, Reginato AM, Wang W. Bone development. *Annu Rev Cell Dev Biol* 2000;16:191-220.
- Gerber HP, Ferrara N. Angiogenesis and bone growth. *Trends Cardiovasc Med* 2000;10:223-228.
- Gerber HP, Vu TH, Ryan AM, Kowalski J, Werb Z, Ferrara N. VEGF couples hypertrophic cartilage remodeling, ossification and angiogenesis during endochondral bone formation. *Nat Med* 1999;5:623-628.
- Zelzer E, Olsen BR. Multiple roles of vascular endothelial growth factor (VEGF) in skeletal development, growth, and repair. *Curr Top Dev Biol* 2005;65:169-187.
- Zelzer E, Mamluk R, Ferrara N, Johnson RS, Schipani E, Olsen BR. VEGFA is necessary for chondrocyte survival during bone development. *Development* 2004;131:2161-2171.
- Zelzer E, McLean W, Ng YS, Fukai N, Reginato AM, Lovejoy S, D'Amore PA, Olsen BR. Skeletal defects in VEGF(120/120) mice reveal multiple roles for VEGF in skeletogenesis. *Development* 2002;129:1893-1904.
- Zelzer E, Glotzer DJ, Hartmann C, Thomas D, Fukai N, Soker S, Olsen BR. Tissue specific regulation of VEGF expression during bone development requires Cbfa1/Runx2. *Mech Dev* 2001;106:97-106.
- Maes C, Carmeliet P, Moermans K, Stockmans I, Smets N, Collen D, Bouillon R, Carmeliet G. Impaired angiogenesis and endochondral bone formation in mice lacking the vascular endothelial growth factor isoforms VEGF164 and VEGF188. *Mech Dev* 2002;111:61-73.
- Riesterer O, Zingg D, Hummerjohann J, Bodis S, Pruschy M. Degradation of PKB/Akt protein by inhibition of the VEGF receptor/mTOR pathway in endothelial cells. *Oncogene* 2004;23:4624-4635.
- Cho H, Thorvaldsen JL, Chu Q, Feng F, Birnbaum MJ. Akt1/PKBalpha is required for normal growth but dispensable for maintenance of glucose homeostasis in mice. *J Biol Chem* 2001;276:38349-38352.
- Chen WS, Xu PZ, Gottlob K, Chen ML, Sokol K, Shiyanova T, Roninson I, Weng W, Suzuki R, Tobe K, Kadowaki T, Hay N. Growth retardation and increased apoptosis in mice with homozygous disruption of the Akt1 gene. *Genes Dev* 2001;15:2203-2208.
- Ulici V, Hoenselaar KD, Agoston H, McErlain DD, Umoh J, Chakrabarti S, Holdsworth DW, Beier F. The role of Akt1 in terminal stages of endochondral bone formation: angiogenesis and ossification. *Bone* 2008;45:1133-1145.
- Kawamura N, Kugimiya F, Oshima Y, Ohba S, Ikeda T, Saito T, Shinoda Y, Kawasaki Y, Ogata N, Hoshi K, Akiyama T, Chen WS, Hay N, Tobe K, Kadowaki T, Azuma Y, Tanaka S, Nakamura K, Chung UI, Kawaguchi H. Akt1 in osteoblasts and osteoclasts controls bone remodeling. *PLoS ONE* 2007;2:e1058.
- Wedge SR, Ogilvie DJ, Dukes M, Kendrew J, Chester R, Jackson JA, Boffey SJ, Valentine PJ, Curwen JO, Musgrove HL, Graham GA, Hughes GD, Thomas AP, Stokes ES, Curry B, Richmond GH, Wadsworth PF, Bigley AL, Hennequin LF. ZD6474 inhibits vascular

- endothelial growth factor signaling, angiogenesis, and tumor growth following oral administration. *Cancer Res* 2002;62:4645–4655.
16. Plaks V, Kalchenko V, Dekel N, Neeman M. MRI analysis of angiogenesis during mouse embryo implantation. *Magn Reson Med* 2006;55:1013–1022.
  17. Dafni H, Landsman L, Schechter B, Kohen F, Neeman M. MRI and fluorescence microscopy of the acute vascular response to VEGF165: vasodilation, hyper-permeability and lymphatic uptake, followed by rapid inactivation of the growth factor. *NMR Biomed* 2002;15:120–131.
  18. Ziv K, Nevo N, Dafni H, Israely T, Granot D, Brenner O, Neeman M. Longitudinal MRI tracking of the angiogenic response to hind limb ischemic injury in the mouse. *Magn Reson Med* 2004;51:304–311.
  19. Israely T, Dafni H, Nevo N, Tsafirri A, Neeman M. Angiogenesis in ectopic ovarian xenotransplantation: multiparameter characterization of the neovasculature by dynamic contrast-enhanced MRI. *Magn Reson Med* 2004;52:741–750.
  20. Dafni H, Kim SJ, Bankson JA, Sankaranarayananpillai M, Ronen SM. Macromolecular dynamic contrast-enhanced (DCE)-MRI detects reduced vascular permeability in a prostate cancer bone metastasis model following anti-platelet-derived growth factor receptor (PDGFR) therapy, indicating a drop in vascular endothelial growth factor receptor (VEGFR) activation. *Magn Reson Med* 2008;60:822–833.
  21. Dafni H, Israely T, Bhujwalla ZM, Benjamin LE, Neeman M. Overexpression of vascular endothelial growth factor 165 drives peritumor interstitial convection and induces lymphatic drain: magnetic resonance imaging, confocal microscopy, and histological tracking of triple-labeled albumin. *Cancer Res* 2002;62:6731–6739.
  22. Dafni H, Gilead A, Nevo N, Eilam R, Harmelin A, Neeman M. Modulation of the pharmacokinetics of macromolecular contrast material by avidin chase: MRI, optical, and inductively coupled plasma mass spectrometry tracking of triply labeled albumin. *Magn Reson Med* 2003;50:904–914.
  23. Russ J, Dehoff R. *Practical stereology*. 2nd ed. Plenum Press: New York; 1999. p 149–181.
  24. Gomberg BR, Saha PK, Wehrli FW. Topology-based orientation analysis of trabecular bone networks. *Med Phys* 2003;30:158–168.
  25. Libicher M, Kasperk C, Daniels M, Hosch W, Kauczor HU, Delorme S. Dynamic contrast-enhanced MRI in Paget's disease of bone—correlation of regional microcirculation and bone turnover. *Eur Radiol* 2008;18:1005–1011.
  26. Bauerle T, Bartling S, Berger M, Schmitt-Graff A, Hilbig H, Kauczor HU, Delorme S, Kiessling F. Imaging anti-angiogenic treatment response with DCE-VCT, DCE-MRI and DWI in an animal model of breast cancer bone metastasis. *Eur J Radiol* 2009;19:2495–2507.
  27. Shih TT, Hou HA, Liu CY, Chen BB, Tang JL, Chen HY, Wei SY, Yao M, Huang SY, Chou WC, Hsu SC, Tsay W, Yu CW, Hsu CY, Tien HF, Yang PC. Bone marrow angiogenesis magnetic resonance imaging in patients with acute myeloid leukemia: peak enhancement ratio is an independent predictor for overall survival. *Blood* 2009;113:3161–3167.
  28. Kanczler JM, Oreffo RO. Osteogenesis and angiogenesis: the potential for engineering bone. *Eur Cell Mater* 2008;15:100–114.
  29. Edwards JR, Williams K, Kindblom LG, Meis-Kindblom JM, Hogendoorn PC, Hughes D, Forsyth RG, Jackson D, Athanasou NA. Lymphatics and bone. *Hum Pathol* 2008;39:49–55.
  30. Steer AC, Carapetis JR. Acute hematogenous osteomyelitis in children: recognition and management. *Paediatr Drugs* 2004;6:333–346.
  31. Yang ZZ, Tschopp O, Di-Poi N, Bruder E, Baudry A, Dummler B, Wahli W, Hemmings BA. Dosage-dependent effects of Akt1/protein kinase B alpha (PKBalpha) and Akt3/PKBgamma on thymus, skin, and cardiovascular and nervous system development in mice. *Mol Cell Biol* 2005;25:10407–10418.
  32. Yang ZZ, Tschopp O, Hemmings-Mieszczyk M, Feng J, Brodbeck D, Perentes E, Hemmings BA. Protein kinase B alpha/Akt1 regulates placental development and fetal growth. *J Biol Chem* 2003;278:32124–32131.
  33. Chen J, Somanath PR, Razorenova O, Chen WS, Hay N, Bornstein P, Byzova TV. Akt1 regulates pathological angiogenesis, vascular maturation and permeability in vivo. *Nat Med* 2005;11:1188–1196.
  34. Petersen W, Tsokos M, Pufe T. Expression of VEGF121 and VEGF165 in hypertrophic chondrocytes of the human growth plate and epiphyseal cartilage. *J Anat* 2002;201:153–157.